

to two copies within the complex (fig. S2A). Fip1 is thought to tether Pap1 to CPF (*13–16*). We also observed subcomplexes that contain Pap1, but not Fip1 (table S2), suggesting that Pap1 may contact other CPF subunits (*16, 17*). The poly(A) polymerase module is analogous to a four-subunit mammalian complex, which is necessary and sufficient for specific *in vitro* polyadenylation (*18*). This suggests that the architecture of yeast and mammalian complexes is highly similar.

NanoESI-MS did not reveal interactions between the three enzymatic modules of CPF. The modules may be held together by hydrophobic interactions that are stable in solution but weakened in the gas phase (*11*). Pull-down assays with subunits from each module revealed potential connections between them (fig. S2B).

To understand the molecular basis of subunit association, we used electron cryomicroscopy (cryo-EM) to study CPF isolated from yeast. This resulted in a three-dimensional (3D) reconstruction at ~ 12 Å resolution (fig. S3). At this resolution, it is not possible to assign densities to

subunits. Moreover, this structure is too small to represent the entire CPF complex.

Next, because of the central role of polyadenylation in 3'-end processing, we developed a strategy to overexpress the polymerase module in insect cells for structural and biochemical characterization. This could be purified with or without the Pap1 subunit, consistent with nanoESI-MS (fig. S4A). We imaged the ~ 200 -kDa recombinant four-subunit complex (Cft1, Pfs2, Yth1, Fip1) using cryo-EM (fig. S4, B and C). We determined a 3D reconstruction of the complex, at an overall resolution of 3.5 Å, allowing us to build atomic models into the density for 1717 amino acids (table S3 and figs. S4 and S5). Prior to this, the only high-resolution structure available for this complex was a crystal structure of 72 amino acids of CPSF30/Yth1 (*19*). The polymerase module is markedly similar to the structure we obtained with the native CPF preparation (fig. S3).

In our cryo-EM map (Fig. 2 and movie S1), three of the four subunits are well ordered: Cft1 (residues 1 to 1357), Pfs2 (residues 27 to 411),

and Yth1 (residues 1 to 94). The C-terminal half of Yth1 (zinc fingers 3 to 5, residues 95 to 208), all of Fip1, and several loops in Cft1 are not visible and are presumably disordered, consistent with predictions (fig. S6A).

Cft1 forms the core of the complex and is composed of three seven-bladed β propellers followed by a C-terminal helical domain. β propeller 1 (BP1) and BP2 are each formed of contiguous sequences. By contrast, BP3 is predominantly C-terminal, but it also contains one β strand from the N terminus and three β strands from the middle of the protein, creating an intertwined and rigid structural core (fig. S6B). The C-terminal helical domain of Cft1 is located at the nexus of the three β propellers, further stabilizing the fold (Fig. 2B).

Our structure reveals an extensive interface between Cft1 and Pfs2, burying >4200 Å² surface area (Fig. 3A). Almost 50 amino acids in the N-terminal region of Pfs2 are inserted into the cavity between Cft1-BP1 and -BP3, forming contacts with the tops of both β propellers (Fig. 3B). A Pfs2 β propeller (fig. S6C) is then positioned

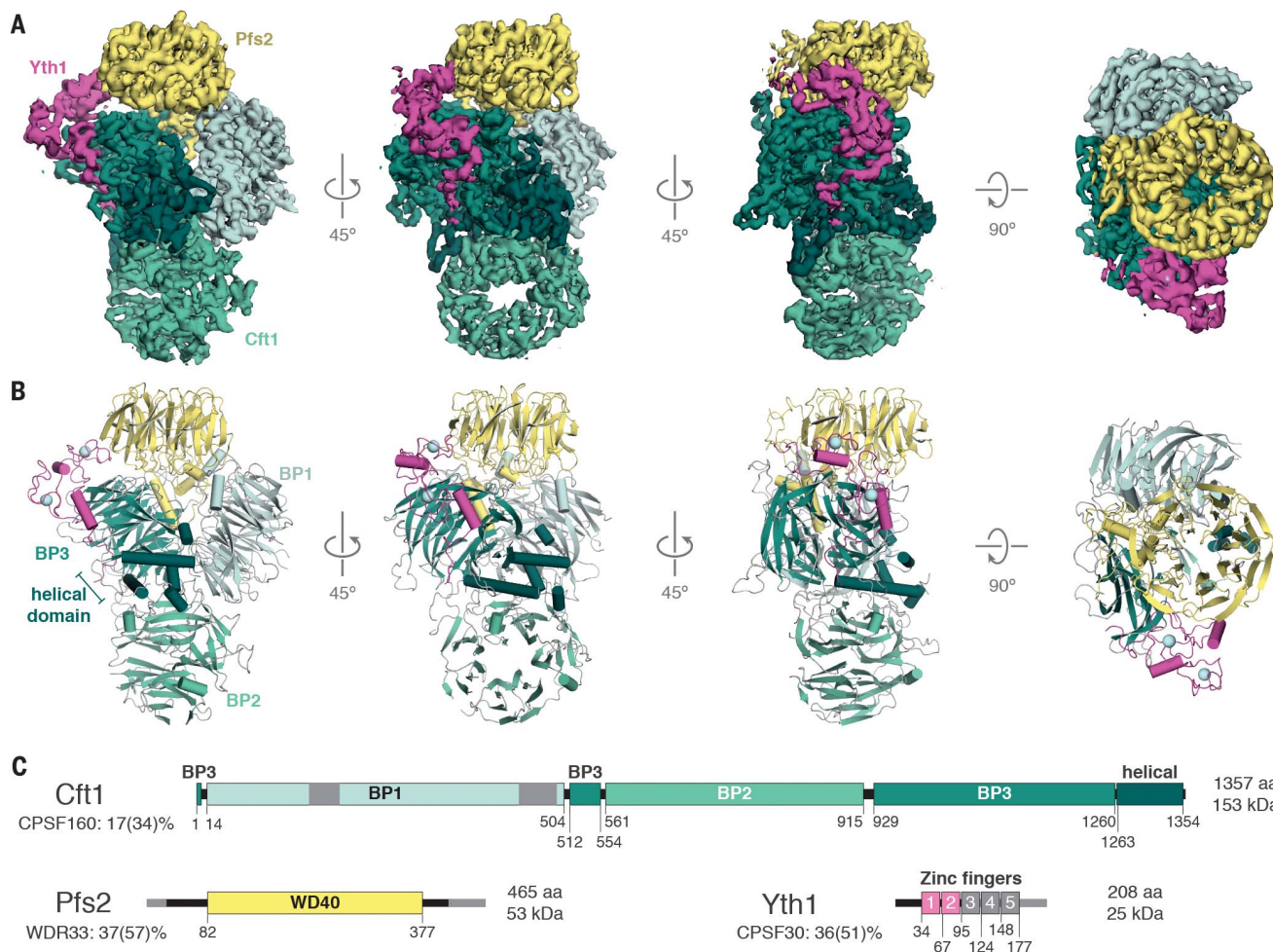


Fig. 2. Cryo-EM of the polymerase module of CPF. (A) Cryo-EM map and (B) cartoon representation of the atomic model of the Cft1-Pfs2-Yth1 complex of the polymerase module. Yth1 (magenta), Pfs2 (yellow), Cft1 (green), and zinc ions (pale cyan) are depicted. The three β -propeller domains of Cft1

(BP1, BP2, and BP3) are colored in different shades. (C) Schematic representation of polymerase module subunits present in the cryo-EM structure, with domain boundaries. Gray regions are not ordered in the cryo-EM map. Human orthologs are given with the percent sequence identity (similarity).

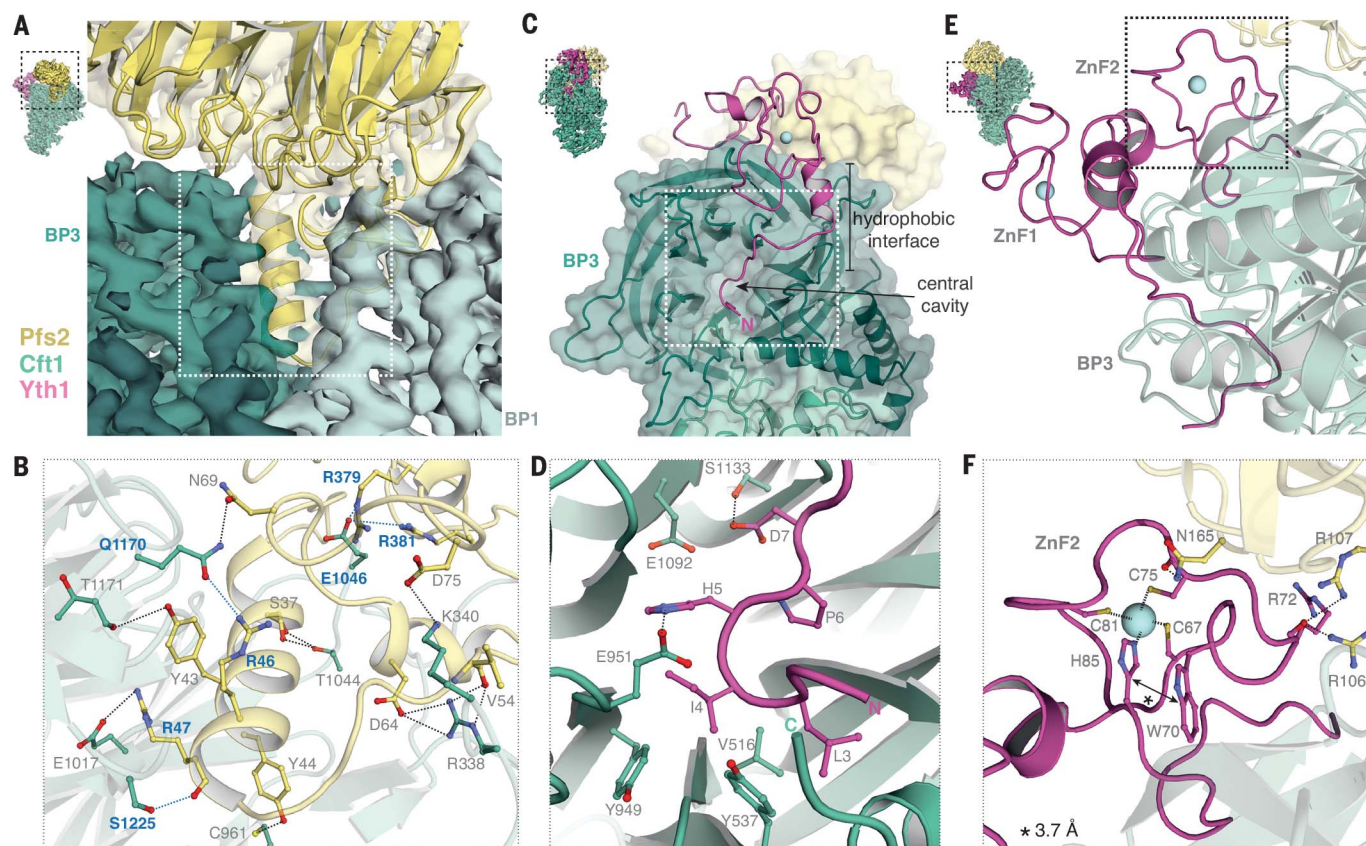


Fig. 3. Protein-protein interactions in the polymerase module. (A and B) Details of the Cft1 (green)–Pfs2 (yellow) interaction. The cryo-EM map of Cft1 is shown (A). Selected interactions with residues conserved in human orthologs are labeled in blue (B). (C to F) Details of Yth1 (magenta) interaction with Pfs2 and Cft1. A surface representation of the Cft1 model is shown (C). Selected electrostatic and hydrophobic interactions are

depicted (D). Zinc ions are in cyan (E). ZnF2 is stabilized by pi stacking between Yth1-H85 and -W70, as well as several hydrogen-bonding interactions between side chains of Pfs2 and backbone atoms of Yth1 (F). Single-letter abbreviations for the amino acid residues are as follows: C, Cys; D, Asp; E, Glu; H, His; I, Ile; K, Lys; L, Leu; N, Asn; P, Pro; Q, Gln; R, Arg; S, Ser; T, Thr; V, Val; W, Trp; and Y, Tyr.

on the top of Cft1 stabilized by loops extending from BP1 and BP3. Many key interactions between these two proteins are conserved in the human orthologs CPSF160 and WDR33 (Fig. 3B and fig. S7).

Yth1 is anchored onto the complex by an extended N-terminal segment that binds in the central cavity of Cft1-BP3 and continues across a hydrophobic external face (Fig. 3, C and D). Next, two of the five Cys-Cys-Cys-His (CCCH) zinc fingers pack into the interface between Cft1 and Pfs2 (Fig. 3, E and F).

We performed cross-linking mass spectrometry to validate our structural model and to determine where Pap1 and Fip1 bind. Inter- and intramolecular cross-links agree with our atomic models, and the crystal structure of Pap1 (fig. S8 and table S4) (20). Fip1 cross-links to the C-terminal part of Yth1 and the polymerase domain of Pap1 (fig. S8B). A previous crystal structure of Pap1 in complex with a peptide of Fip1 (15) revealed molecular details of their interaction, but Pap1 also cross-links to the C-terminal helical domain of Cft1, ZnF1 of Yth1, and the C-terminal region of Pfs2 (fig. S8). Together, these data

suggest that the flexible C-terminal half of Yth1 binds the intrinsically disordered protein Fip1, which in turn flexibly tethers Pap1 to the complex, allowing conformational freedom to add long poly(A) tails onto diverse RNA substrates.

The cryo-EM structure of the Cft1–Pfs2–Yth1 complex of the polymerase module has a markedly similar architecture to the eukaryotic DDB1–DDB2 and SF3b complexes (21–24) (Fig. 4, A to C). DDB1–DDB2 recognizes ultraviolet-damaged DNA and acts as an adapter for a cullin-RING E3 ubiquitin ligase to trigger nucleotide excision repair. SF3b is a multiprotein assembly containing the Rse1/SF3b130 scaffold protein, which forms part of the U2snRNP complex essential for pre-mRNA splicing and branch site recognition.

DDB1 and Rse1 both contain three β propellers followed by a C-terminal α -helical domain, with the same fold as Cft1, and the three proteins show weak sequence homology (~15% sequence identity). Thus, all three complexes use similar scaffold proteins (DDB1, Rse1, or Cft1) to assemble a rigid and structurally stable complex. Their interaction partners (DDB2, Hsh155/Rds3, or

Pfs2) bind in the same cavity between BP1 and BP3, with a similar binding mode that involves α helices, but the exact interaction mechanism is not conserved (Fig. 4, A to C). Like DDB1–DDB2 and SF3b, Cft1 may bind additional subunits through its β propellers.

DDB1–DDB2 and SF3b directly bind nucleic acid. The polymerase module also binds RNA in a gel-shift assay (fig. S9A). The surface of Pfs2 equivalent to the DDB2 DNA binding site contains a cluster of conserved lysines, arginines, and aromatic residues that could form an RNA interaction surface (fig. S9, B to D). This Pfs2 surface lies adjacent to the RNA-binding ZnF2 of Yth1 (25–27) and together, they might constitute a composite RNA-binding platform (Fig. 4A) that is disrupted in viral infections (fig. S9E).

Intact CPF requires the accessory cleavage factors (CF) IA and IB for efficient and specific polyadenylation (28–30). Addition of recombinant CF IA (but not CF IB) stimulates the polyadenylation activity of the polymerase module and intact CPF (Fig. 4D and fig. S10, A to C). CF IA has no effect on isolated Pap1 (fig. S10D), underscoring the functional importance of the other subunits.

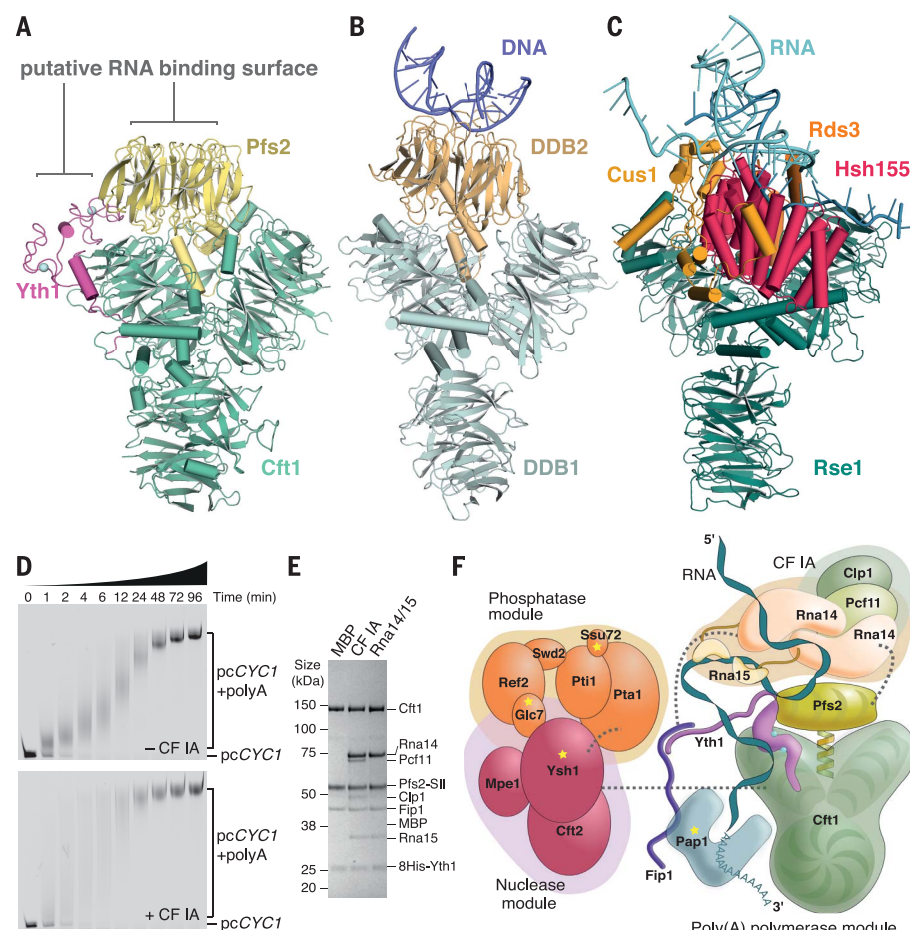


Fig. 4. The polymerase module acts as a hub to bring together Pap1, RNA, and accessory factors. (A to C) The Cft1–Pfs2–Yth1 complex of the polymerase module (A) is structurally similar to the DDB1–DDB2 DNA repair [PDB: 3ei3 (B)] and SF3b splicing [PDB: 5gm6 (C)] complexes. (D) Polyadenylation of a fluorescently labeled 42-nucleotide precleaved (pc) CYC1 RNA by the polymerase module (with and without CF IA) analyzed by 15% denaturing urea PAGE. (E) Coomassie-stained SDS-PAGE of pull-down experiment showing immobilized polymerase module after incubation with purified maltose-binding protein (MBP), CF IA, or Rna14–Rna15. (F) Model for the 3'-end processing machinery obtained by combining data from nanoESI-MS, cryo-EM, cross-linking–mass spectrometry, and in vitro pull-down assays. Yellow stars denote enzymes.

CF IA is composed of four different protein subunits—a heterotetramer of Rna14–Rna15 and a heterodimer of Pcf11–Clp1. Rna14–Rna15 was sufficient to stimulate polyadenylation (Fig. S10E). Moreover, the CF IA complex, and specifically the Rna14–Rna15 subcomplex, binds to the polymerase module in pull-down assays (Fig. 4E and Fig. S10F).

The arrangement of CPF, in which its enzymatic activities are segregated into three modules, suggests that coupling between the enzymes is not through intimate, stable contacts and may be dynamic. CF IA likely stimulates polyadenylation by contributing additional RNA binding sites. Together, Pfs2, Yth1, and CF IA could stably bring specific RNA sequences to the complex. This would allow Pap1, which is flexibly tethered to the complex by the intrinsically disordered protein Fip1, to access a variety of different RNA substrates for efficient and controlled polyadenylation. Thus,

the polymerase module acts as a hub to bring together Pap1, substrate RNA, and CF IA (Fig. 4F). Moreover, by tethering these components together with the nuclease and phosphatase modules of CPF, it would facilitate accurate 3'-end processing, and coordination with transcription.

REFERENCES AND NOTES

1. J. Zhao, M. M. Kessler, C. L. Moore, *J. Biol. Chem.* **272**, 10831–10838 (1997).
2. P. J. Preker, M. Ohnacker, L. Minvielle-Sebastia, W. Keller, *EMBO J.* **16**, 4727–4737 (1997).
3. M. Ohnacker, S. M. Barabino, P. J. Preker, W. Keller, *EMBO J.* **19**, 37–47 (2000).
4. A.-C. Gavin et al., *Nature* **415**, 141–147 (2002).
5. E. Nedeia et al., *J. Biol. Chem.* **278**, 33000–33010 (2003).
6. X. He, C. Moore, *Mol. Cell* **19**, 619–629 (2005).
7. A. Schrieck et al., *Nat. Struct. Mol. Biol.* **21**, 175–179 (2014).
8. S. Danckwardt, M. W. Hentze, A. E. Kulozik, *EMBO J.* **27**, 482–498 (2008).
9. C. Mayr, D. P. Bartel, *Cell* **138**, 673–684 (2009).

10. M. E. Nemeroff, S. M. Barabino, Y. Li, W. Keller, R. M. Krug, *Mol. Cell* **1**, 991–1000 (1998).
11. H. Hernández, C. V. Robinson, *Nat. Protoc.* **2**, 715–726 (2007).
12. A. Zhelkovsky et al., *RNA* **12**, 435–445 (2006).
13. P. J. Preker, J. Lingner, L. Minvielle-Sebastia, W. Keller, *Cell* **81**, 379–389 (1995).
14. S. Helmling, A. Zhelkovsky, C. L. Moore, *Mol. Cell. Biol.* **21**, 2026–2037 (2001).
15. G. Meinke et al., *Biochemistry* **47**, 6859–6869 (2008).
16. C. Ezeokonkwo, A. Zhelkovsky, R. Lee, A. Bohm, C. L. Moore, *RNA* **17**, 652–664 (2011).
17. K. G. Murthy, J. L. Manley, *Genes Dev.* **9**, 2672–2683 (1995).
18. L. Schönemann et al., *Genes Dev.* **28**, 2381–2393 (2014).
19. K. Das et al., *Proc. Natl. Acad. Sci. U.S.A.* **105**, 13093–13098 (2008).
20. J. Bard et al., *Science* **289**, 1346–1349 (2000).
21. T. Li, X. Chen, K. C. Garbutt, P. Zhou, N. Zheng, *Cell* **124**, 105–117 (2006).
22. A. Scrima et al., *Cell* **135**, 1213–1223 (2008).
23. C. Yan, R. Wan, R. Bai, G. Huang, Y. Shi, *Science* **353**, 904–911 (2016).
24. C. Cretu et al., *Mol. Cell* **64**, 307–319 (2016).
25. S. M. Barabino, M. Ohnacker, W. Keller, *EMBO J.* **19**, 3778–3787 (2000).
26. Y. Tachashi, S. Helmling, C. L. Moore, *Nucleic Acids Res.* **31**, 1744–1752 (2003).
27. S. L. Chan et al., *Genes Dev.* **28**, 2370–2380 (2014).
28. L. Minvielle-Sebastia, P. J. Preker, W. Keller, *Science* **266**, 1702–1705 (1994).
29. M. M. Kessler, J. Zhao, C. L. Moore, *J. Biol. Chem.* **271**, 27167–27175 (1996).
30. M. M. Kessler et al., *Genes Dev.* **11**, 2545–2556 (1997).

ACKNOWLEDGMENTS

We thank M. Webster, C. Savva, A. Boland, R. Fernández-Leiro, T. Martin, G. Murshudov, S. Scheres, A. Brown, C. Russo, K. Naydenova, A. Yewdall, A. Kelley, Laboratory of Molecular Biology (LMB) electron microscopy facility, and LMB scientific computation for assistance and advice; and D. Barford, A. Carter, and M. Babu for comments on the manuscript. This work was supported by European Molecular Biology Organization Long-Term Fellowship ALTF66-2015 cofunded by the European Commission (LTFCONFUND2013, GA-2013-609409) through Marie Curie Actions (to A.C.); Gates Cambridge (to A.K.); the European Research Council under the European Union's Seventh Framework Programme (FP7/2007–2013)–European Research Council (ERC) grant 261151 (to L.A.P.); the European Union's Horizon 2020 research and innovation programme (ERC grant 725685) (to L.A.P.); ERC grant no. 695511 (ENABLE) (to C.V.R.); and Medical Research Council (MRC) grants MC_U105192715 (L.A.P.) and MC_U105185859 (to M. Babu). We acknowledge Diamond Light Source for access to eBIC (proposal EMI5622) funded by the Wellcome Trust, MRC, and Biotechnology and Biological Sciences Research Council. Cryo-EM density maps are deposited in the Electron Microscopy Data Bank (EMD-3908), and atomic coordinates are deposited in the Protein Data Bank (PDB) (6EOJ). Reagents are available upon request from L.A.P. under a material transfer agreement with MRC. This work is licensed under a Creative Commons Attribution 4.0 International (CC BY 4.0) license, which permits unrestricted use, distribution, and reproduction in any medium, provided the original work is properly cited. To view a copy of this license, visit <http://creativecommons.org/licenses/by/4.0/>. This license does not apply to figures/photos/artwork or other content included in the article that is credited to a third party; obtain authorization from the rights holder before using such material.

SUPPLEMENTARY MATERIALS

www.sciencemag.org/content/358/6366/1056/suppl/DC1
Materials and Methods
Figs. S1 to S10
Tables S1 to S4
References (31–76)
Movie S1
Additional Data S1

11 August 2017; accepted 12 October 2017
Published online 26 October 2017
10.1126/science.aao6535

Architecture of eukaryotic mRNA 3'-end processing machinery

Ana Casañal, Ananthanarayanan Kumar, Chris H. Hill, Ashley D. Easter, Paul Emsley, Gianluca Degliesposti, Yuliya Gordiyenko, Balaji Santhanam, Jana Wolf, Katrin Wiederhold, Gillian L. Dornan, Mark Skehel, Carol V. Robinson and Lori A. Passmore

Science **358** (6366), 1056-1059.

DOI: 10.1126/science.aao6535 originally published online October 26, 2017

Structural basis for mRNA 3'-end processing

The eukaryotic mRNA 3'-end processing machinery interacts with the transcription machinery and adds the polyadenylation tail on the mRNA substrate. Casañal *et al.* used cryo-electron microscopy, mass spectrometry, and biochemical reconstitutions to show that the mRNA 3'-end processing machinery is organized into nuclease, polymerase, and phosphatase modules. The polymerase module of the complex acts as a hub to bring the RNA substrate and the accessory factors together to achieve efficient and controlled polyadenylation coordinated with transcription.

Science, this issue p. 1056

ARTICLE TOOLS

<http://science.sciencemag.org/content/358/6366/1056>

SUPPLEMENTARY MATERIALS

<http://science.sciencemag.org/content/suppl/2017/10/25/science.aao6535.DC1>

REFERENCES

This article cites 74 articles, 25 of which you can access for free
<http://science.sciencemag.org/content/358/6366/1056#BIBL>

PERMISSIONS

<http://www.sciencemag.org/help/reprints-and-permissions>

Use of this article is subject to the [Terms of Service](#)